



Vector angle grouping-based solution separation for multipath/NLOS detection and exclusion with the enhancement of doppler test

Jin Chang¹ · Xingqun Zhan¹ · Yawei Zhai¹ · Shizhuang Wang¹ · Kui Lin¹ · Rong Yang¹

Received: 25 June 2021 / Accepted: 6 July 2022 / Published online: 10 August 2022

© The Author(s), under exclusive licence to Springer-Verlag GmbH Germany, part of Springer Nature 2022

Abstract

In urban areas, global navigation satellite system (GNSS) measurements are susceptible to multipath and non-line-of-sight (NLOS) effects, significantly degrading GNSS performance. Nowadays, multipath/NLOS effects have become the main cause of GNSS measurement fault in an urban environment. Our work mainly focuses on improving GNSS performance in urban areas without using any additional sensors. To achieve this, Doppler test-enhanced fault detection and exclusion (FDE) scheme is proposed to mitigate the influence of multipath/NLOS effects on GNSS positioning. The research is conducted in two folds. First, according to vector angle grouping (VAG) and multiple hypothesis solution separation (MHSS), the fault mode determination process is described. Since the spatial characteristic of multipath/NLOS effects are considered, the fault mode determined by VAG is able to monitor multiple measurement faults caused by multipath/NLOS effects. Second, by introducing Doppler test, Doppler test-enhanced FDE scheme is designed. The proposed FDE scheme combines VAG-based MHSS FDE and the continuity of users' motion, which can obtain more accurate exclusion options. Experiments are carried out based on the open-source dataset, UrbanNav. The results suggest that the proposed algorithm can improve the navigation accuracy about 50% over the traditional receiver autonomous integrity monitoring-based Consistency Check method.

Keywords GNSS · Multipath/NLOS effects · Doppler test · Fault detection and exclusion · Multiple hypothesis solution separations

Introduction

Due to the frequent occurrence of signal reflection and diffraction in urban environments (Morales 2011), global navigation satellite system (GNSS) performance can be significantly affected by multipath and non-line-of-sight (NLOS) effects. GNSS signals disturbed by multipath/NLOS effects are known as multipath and NLOS signals. Among them, the multipath signal is a superposition of direct and reflected signals, and NLOS signal only contains reflected signal (Adjrad and Groves 2017; Grewal et al. 2007). These contaminated signals can distort the correlator output of GNSS receiver, causing errors in code and carrier phase measurements (Grewal et al. 2007; McGraw et al. 2019). Even for high-accuracy positioning techniques, multipath/NLOS effects still strongly influence them. Meanwhile, since

the signal reflection and diffraction are closely related to the surrounding environment, differential positioning techniques cannot eliminate GNSS measurement error in urban areas (Karaim et al. 2018). In some severe conditions, multipath/NLOS effects can result in measurement errors up to 100 m (Borre 2007). At present, multipath/NLOS effects have become the major challenge limiting GNSS applications in urban areas.

Multipath/NLOS effects produce the large measurement error and are the main cause of measurement fault in urban environments. To mitigate Multipath/NLOS effects, existing studies can be classified into three categories:

1. The first category is to change the antenna and receiver design. Chock ring antenna and correlator design of GNSS receiver tracking loop are two examples of multipath effects mitigation (Hofmann-Wellenhof et al. 2007; Dierendonck et al. 1992). However, these methods are not practical for users equipped with traditional GNSS hardware.

✉ Xingqun Zhan
xqzhan@sjtu.edu.cn

¹ School of Aeronautics and Astronautics, Shanghai Jiao Tong University, Shanghai, China

2. The second category is to utilize additional sensors or prior information of urban environments. Marais et al. (2005) and Suzuki (2019) proposed NLOS detection methods using image sensors. Meguro et al. (2009) used an omnidirectional Far-Infrared (FIR) camera to mitigate multipath effects. Moreover, Zhang et al. (2019a, b) used 3D city model to correct multipath and NLOS effects. However, the additional sensors increase the cost of multipath/NLOS mitigation, and the mitigation method based on prior information (such as 3D city model) is only available in specific scenes.
3. The third category is to make full use of redundant data from the GNSS receiver to exclude contaminated measurements. Zhang et al. (2019a, b) presented a technique to detect measurements interfered by multipath effects with dual-frequency C/N0 data. However, this method requires at least dual-frequency GNSS measurements, which are difficult to obtain in complex urban areas. In addition, Hsu et al. (2017) put forward the Consistency Check algorithm to improve GNSS performance in urban areas. Based on receiver autonomous integrity monitoring (RAIM), the Consistency Check method can detect and exclude measurements contaminated by multipath/NLOS effects. Compared with the first method in this category, the Consistency Check method performs better, even without the dual-frequency measurements.

In contrast with methods in the first and second categories, the Consistency Check method not only avoids adding large complex equipment to the antenna or receiver (Strode and Groves 2016) but also expends the application scope of the mitigation algorithm. Though the Consistency Check method has advantages over other methods, the urban GNSS data test shows that large positioning errors still exist in the positioning results of middle or deep urban environments. Therefore, the detection and exclusion effectiveness of the Consistency Check method still needs to be improved.

Advanced receiver autonomous integrity monitoring (RAIM) aims to provide integrity performance analysis for navigation systems in civil aviation (Pan et al. 2019). Since the multiple hypothesis solution separation (MHSS) can monitor the simultaneous multiple satellite faults in navigation systems (Pervan et al. 1998), MHSS has become the basis of ARAIM. According to theoretical analysis (Joerger et al. 2014), the solution separation-based fault detection has a lower detection threshold than the RAIM-based fault detection. Therefore, the solution separation method can improve the detection efficiency of the Consistency Check method.

The key idea of solution separation is to determine the fault modes. However, for MHSS fault detection and exclusion (FDE) in urban areas, the fault modes cannot be obtained in terms of the principles in ARAIM because the

fault probability of GNSS measurement is uncertain. Therefore, vector angle grouping (VAG) is proposed to determine the fault modes for MHSS FDE. Since VAG exploits the relationship of measurement errors caused by multipath/NLOS effects between different satellites, VAG-based MHSS FDE can be applied in the urban environment. In fact, the detection and exclusion criterion of VAG-based MHSS FDE could fail under multi-GNSS fault condition, leading to the large deviation between the positioning result of adjacent epochs. To avoid miss detection and wrong exclusion events, the Doppler test is introduced. The proposed Doppler test-enhanced FDE scheme is supposed to achieve better performance than the Consistency Check method.

MHSS FDE algorithm in ARAIM

For GNSS pseudorange positioning, the linearized observation equation is given by (1):

$$\mathbf{Z} = \mathbf{Hx} + \mathbf{v} + \mathbf{f} \quad (1)$$

where \mathbf{Z} is the $n \times 1$ observation vector. n represents the number of satellite. \mathbf{H} is the $n \times (m+3)$ geometric matrix. m represents the number of constellations. \mathbf{x} is the vector of $(m+3)$ unknown and its estimated value is $\hat{\mathbf{x}}_0$. \mathbf{v} is the $n \times 1$ error vector, which can be bounded by a normal distribution $\mathbf{v} \sim N(\mathbf{b}, \mathbf{W})$ (Zhai et al. 2020). \mathbf{W} is the diagonal covariance matrix of measurement errors. \mathbf{b} is bias vector with each element as $\pm b_{norm}$. \mathbf{f} is the $n \times 1$ fault vector, where the elements are zeros if the measurements are fault free. Weighted least square (WLS) estimation is implemented to estimate \mathbf{x} in (1). The solution of (1) is given by:

$$\hat{\mathbf{x}}_0 = (\mathbf{H}^T \mathbf{W}^{-1} \mathbf{H})^{-1} \mathbf{H}^T \mathbf{W}^{-1} \mathbf{Z} = \mathbf{S}_0 \mathbf{Z} \quad (2)$$

where $\hat{\mathbf{x}}_0$ is the estimate of \mathbf{x} . The first step of ARAIM MHSS FDE is determining the monitored fault modes and calculating subset solutions. For civil aviation, the principles of fault mode determination are based on the probability of satellite fault and constellation fault (Zhai et al. 2020). After determining the fault mode (single-satellite fault mode or multi-satellite fault mode), the number of subset solution \tilde{n} can be calculated. Subsequently, the MHSS fault detection can be implemented. Assuming that only single-satellite fault is monitored, in this case, \tilde{n} equals n . The test statistic $\Delta \mathbf{x}_i$ of fault mode i can be denoted as:

$$\Delta \mathbf{x}_i = |\hat{\mathbf{x}}_i - \hat{\mathbf{x}}_0| \quad (3)$$

In (3), $\hat{\mathbf{x}}_i$ is the subset solution which can be expressed as:

$$\hat{\mathbf{x}}_i = (\mathbf{H}^T \mathbf{W}_i^{-1} \mathbf{H})^{-1} \mathbf{H}^T \mathbf{W}_i^{-1} \mathbf{Z} = \mathbf{S}_i \mathbf{Z} \quad (4)$$

where \mathbf{W}_i is defined as \mathbf{W} with the i -th diagonal element equals to 0. i corresponds to the i -th single-satellite fault mode in MHSS fault detection.

When none of the test statistics $\Delta\mathbf{x}_i$ exceeds its corresponding threshold T_i , this indicates the measurements are fault free. For detection threshold T_i , it can be calculated by the following equation:

$$T_i = Q^{-1} \left(\frac{P_{FA}}{d\tilde{n}P_{FF}} \right) \sigma_i \quad (5)$$

where d equals 2 or 4 for vertical direction and horizontal direction. σ_i is Standard Deviation (STD) of $\Delta\mathbf{x}_i$ in horizontal or vertical direction. P_{FA} is probability of false alert. Q^{-1} is the inverse of right tail probability function of normal distribution (Blanch et al. 2012). P_{FF} is the probability of the fault-free condition.

Once a measurement fault is detected, the MHSS fault exclusion is operated. The test statistic of MHSS fault exclusion is given by:

$$\Delta\mathbf{x}_{j,i} = |\hat{\mathbf{x}}_{j,i} - \hat{\mathbf{x}}_i|, j \neq i \quad (6)$$

where the sub-subset solution $\hat{\mathbf{x}}_{j,i}$ is denoted as follows:

$$\hat{\mathbf{x}}_{j,i} = (\mathbf{H}^T \mathbf{W}_{j,i}^{-1} \mathbf{H})^{-1} \mathbf{H}^T \mathbf{W}_{j,i}^{-1} \mathbf{Z} = \mathbf{S}_{j,i} \mathbf{Z}, j \neq i \quad (7)$$

$\mathbf{W}_{j,i}$ is defined as \mathbf{W} with the j -th and i -th diagonal elements equals to 0. j corresponds to the j -th single-satellite fault mode of MHSS fault exclusion ($j \neq i$).

For fault mode i in MHSS fault detection, if all test statistics $\Delta\mathbf{x}_{j,i}$ ($\forall j \leq n, j \neq i$) are less than their corresponding thresholds $T_{j,i}$, this indicates i is the correct exclusion option. The exclusion threshold $T_{j,i}$ is denoted by the following equation:

$$T_{j,i} = Q^{-1} \left(\frac{P_{FDNE}}{d\tilde{n}(\tilde{n}-1)P_i} \right) \sigma_{j,i} \quad (8)$$

where $\sigma_{j,i}$ is STD of $\Delta\mathbf{x}_{j,i}$ in the horizontal or vertical direction. P_{FDNE} is probability of fault detection and not exclusion (Blanch et al. 2012). P_i is the probability of the i -th fault mode.

Faulty GNSS measurements detection and exclusion in urban area based on MHSS

RAIM MHSS can detect and exclude GNSS faulty measurements in civil aviation, but in urban areas, it is difficult to determine the fault modes of ARAIM MHSS because the fault probability of GNSS measurement is uncertain. As multipath/NLOS effects are the main cause of GNSS

measurement fault in urban environments, VAG is proposed to determine the fault modes using the relationship between the measurement errors of different satellites and their vector angles. When the fault modes are determined, MHSS FDE for urban areas is implemented to improve the performance of GNSS.

Vector angle grouping

Fault mode determination function in MHSS FDE is based on the prior probability of fault on satellite and constellation. For ARAIM algorithm in civil aviation, these probabilities are obtained from a large amount of GNSS data (Walter et al. 2019). However, in urban areas, the fault probability of GNSS measurement is highly correlated with the surrounding environment due to the interference of multipath/NLOS effects. In this case, the fault probability is no longer a definite value. vector angle grouping (VAG) is proposed to determine the fault modes in the urban environment.

Multipath/NLOS effects are generally considered to be related to elevation angle because low-elevation-angle signals are more likely to be received via reflections from vertical surfaces (McGraw et al. 2020). In fact, high-elevation-angle signals can still be contaminated by NLOS effect in urban areas (Hsu 2018). Hence, only using elevation angle information cannot precisely describe the feature of the multipath/NLOS effect.

For multipath/NLOS effects are related to surrounding environments, the measurements of satellites spatially close to each other are more likely to be contaminated by multipath/NLOS errors with the same magnitude. Using the spatial correlation of multipath/NLOS effects, VAG combines both elevation and azimuth angles to determine fault modes. The definition of vector angle is given by (9):

$$\cos \theta = \frac{\vec{\mathbf{OS}_1} \cdot \vec{\mathbf{OS}_2}}{\|\vec{\mathbf{OS}_1}\| \|\vec{\mathbf{OS}_2}\|} = \langle \vec{\mathbf{OS}_1}, \vec{\mathbf{OS}_2} \rangle \quad (9)$$

where θ is the vector angle and $\cos\theta$ represents the Correlation Coefficient Value (CCV) in mathematics. $\vec{\mathbf{OS}_1}$ and $\vec{\mathbf{OS}_2}$ are two vectors whose origins locate at the position of GNSS antenna and endpoints locate at the position of different satellites. $\langle \rangle$ is the symbol for calculating the cosine value of vector angles between $\vec{\mathbf{OS}_1}$ and $\vec{\mathbf{OS}_2}$. Figure 1 is the schematic of vector angle.

To validate the relationship between multipath/NLOS effects and vector angle, the real-time GNSS dataset UrbanNav collected from Odaiba and Shinjuku (which will be described in detail in the experimental section) is utilized. First, measurement errors caused by multipath/NLOS effects can be obtained by double difference and the ground truth. Second, the mean value of

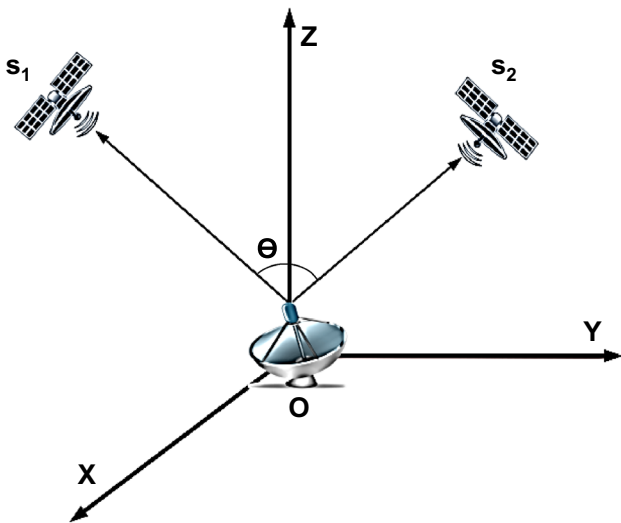


Fig. 1 Vector angle schematic. s_1 and s_2 represent the position of different satellites. O represents the position of the GNSS antenna

multipath/NLOS difference M is defined as the difference of ranging error between different satellites under a certain CCV over a period of time. Assuming that satellites satisfying predefined CCV can be found in each epoch, M is given by:

$$M = \frac{1}{N} \sum_{i=1}^{i=N} \frac{1}{K} \sum_{j=1}^{j=K} |MP_{j,1}(i \cdot \delta t) - MP_{j,2}(i \cdot \delta t)| \quad (10)$$

However, if satellites satisfying predefined CCV can be found only in some epochs, M is given by:

$$M = \frac{1}{N_F} \sum_{i=1}^{i=N} \frac{1}{K} \sum_{j=1}^{j=K} |MP_{j,1}(i \cdot \delta t) - MP_{j,2}(i \cdot \delta t)| \quad (11)$$

where $MP_{j,1}(i \cdot \delta t)$ and $MP_{j,2}(i \cdot \delta t)$ are measurement errors caused by multipath/NLOS effects at epoch $i\delta t$ under a certain CCV. δt is sampling interval. The subscripts 1 and 2 represent two different satellites. A pair of $MP_{j,1}(i \cdot \delta t)$ and $MP_{j,2}(i \cdot \delta t)$ used to calculate the value of $MP_{j,1}(i \cdot \delta t) - MP_{j,2}(i \cdot \delta t)$ are denoted as MP -pair. K is the number of MP -pair at epoch $i\delta t$. For instance, assuming there are s satellites at epoch $i\delta t$ and the CCV between any two satellites equals the predefined value, in this case, K equals C_s^2 . N is the number of sampling points of the dataset. N_F is the number of epochs used to calculate M when satellites satisfying the predefined CCV can be found only in some epochs.

The CCV of $MP_{j,1}(i \cdot \delta t)$ and $MP_{j,2}(i \cdot \delta t)$ is given by:

$$C_j = \left\langle \vec{OS}_{j,1}, \vec{OS}_{j,2} \right\rangle \quad (12)$$

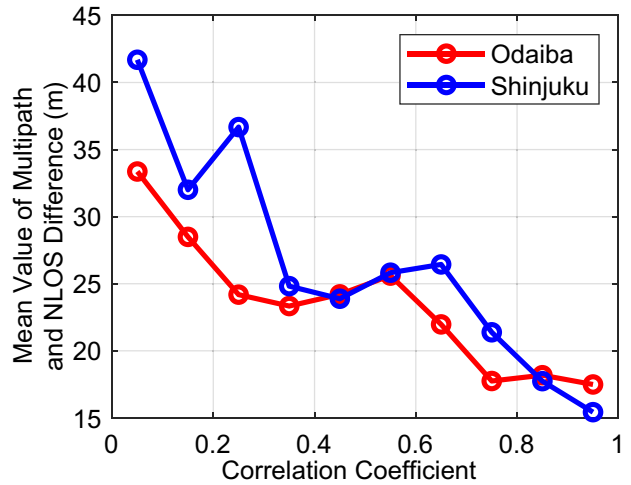


Fig. 2 Relationship between multipath/NLOS difference and CCV. The red line and blue line represent the multipath/NLOS difference under different CCV in Odaiba and Shinjuku, which are calculated by the real-time data

where the origins of $\vec{OS}_{j,1}$ and $\vec{OS}_{j,2}$ are the same as \vec{OS}_1 and \vec{OS}_2 in (9). The endpoints of $\vec{OS}_{j,1}$ and $\vec{OS}_{j,2}$ locate at the position of different satellites whose measurement errors correspond to $MP_{j,1}(i\delta t)$ and $MP_{j,2}(i\delta t)$, respectively. Since over 90% of CCVs are higher than 0, we only analyze the data with CCV higher than 0.

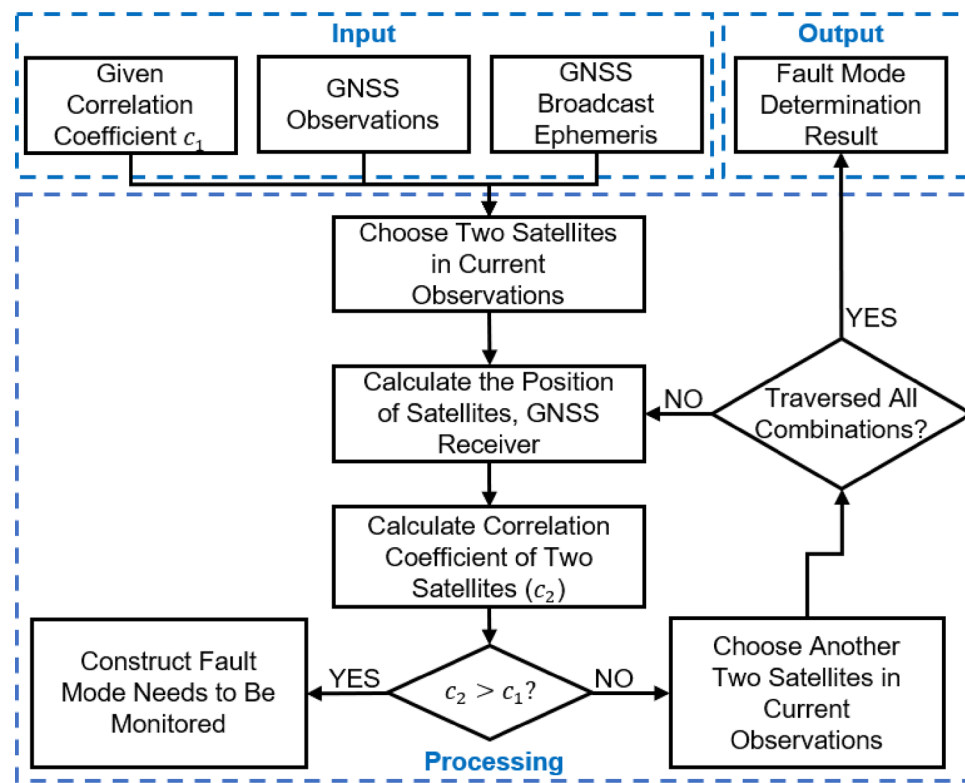
Figure 2 depicts the relationship between multipath/NLOS difference M and CCV. When CCV is close to 1 (vector angle is close to 0), multipath/NLOS difference appears to be small. Therefore, in urban areas (Odaiba and Shinjuku), due to the interference of multipath/NLOS effects, measurement errors of satellites spatially close to each other have a similar magnitude. Based on the results in Fig. 2, for MHSS in urban environment, satellites spatially close to each other can be included in the same fault mode.

The process of Fault mode determination is shown in Fig. 3. When a certain CCV C_1 is given, this process aims to choose satellites with CCV larger than or equal to C_1 and construct the fault mode with these satellites. When CCVs between one satellite and several satellites are larger than or equal to C_1 , these satellites should be classified into one fault mode.

VAG-based MHSS fault detection

VAG-based MHSS fault detection is similar to fault detection in ARAIM algorithm. The difference lies in the calculation of test threshold. For the fault detection in ARAIM algorithm, P_{FA} can be rewritten as (Joerger et al. 2014):

Fig. 3 Fault mode determination flowchart. The fault mode determination process is to find satellites with similar multipath/NLOS error magnitude and classify these satellites into one fault mode



$$P_{FA} = \sum_{i=1}^{\tilde{n}} P(|\Delta_i| > T_i | H_0) P_{FF} \quad (13)$$

where H_0 represents fault-free condition. (12) can be rewritten as:

$$\frac{P_{FA}}{\tilde{n} P_{FF}} = P(|\Delta_i| > T_i | H_0) \quad (14)$$

when assuming that P_{FA} is evenly allocated to each solution.

Under the fault-free condition (H_0), Δ_i obeys Gaussian distribution with 0 mean. For P_{FF} is impossible to be acquired in urban areas, we assume that the probability of GNSS measurement fault is low under the fault-free condition, and then maximize P_{FF} to obtain a looser threshold. The threshold $T_{i,D}$ is given by:

$$T_{i,D} = Q^{-1} \left(\frac{P_{FA}}{d\tilde{n}} \right) \sigma_i \quad (15)$$

Since P_{FF} is maximized, threshold $T_{i,D}$ is larger than T_i . Flowchart of VAG-Based MHSS fault detection is shown in Fig. 4. VAG-Based MHSS fault detection requires at least seven satellites to be applied for three-constellation positioning.

VAG-based MHSS fault exclusion

In ARAIM fault exclusion, P_{FDNE} is introduced to calculate the exclusion threshold, which is expressed as (Joerger et al. 2014):

$$P_{FDNE} = \sum_{j=1}^{\tilde{n}} \sum_{i=1, i \neq j}^{\tilde{n}-1} P(|\Delta_{j,i}| > T_{j,i} | H_0) P_j \quad (16)$$

where P_j is the probability of the j -th fault mode for fault exclusion. Since VAG-Based MHSS fault detection assumes that the probability of GNSS measurement fault is low under the fault-free condition, the threshold for VAG-Based MHSS fault exclusion cannot be obtained by maximizing P_j . Therefore, VAG-Based fault exclusion is based on the VAG-Based fault detection. For fault mode with the largest normalized test statistic $\frac{\Delta x_i}{\sigma_i}$ is more likely to be the right exclusion option (Zhai et al. 2018), VAG-Based MHSS fault exclusion is shown in Fig. 5.

Fault-free error model

The fault-free error model in MHSS is of great importance because it determines the correctness of σ_i and FDE threshold. The fault-free error model in ARAIM is designed for civil aviation, which Boeing and Honeywell have validated

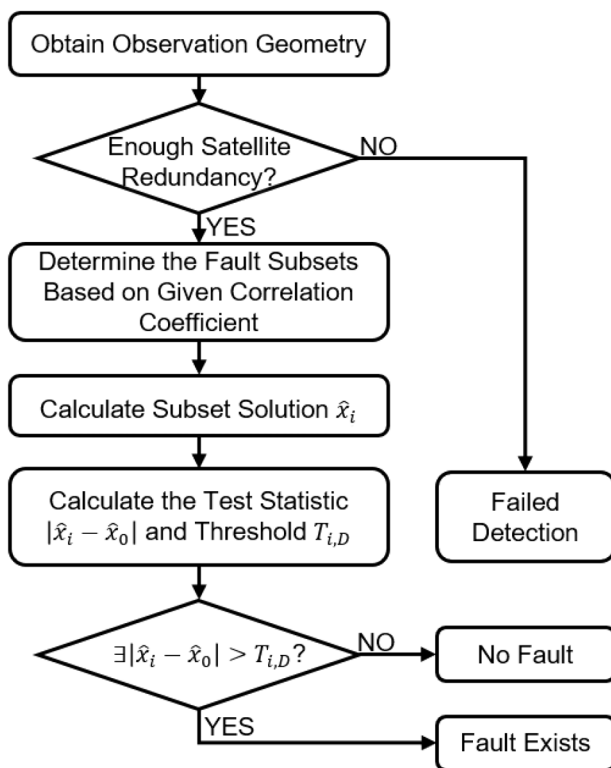


Fig. 4 Flowchart of VAG-Based MHSS fault detection. This function can implement only when the satellite redundancy requirement is satisfied

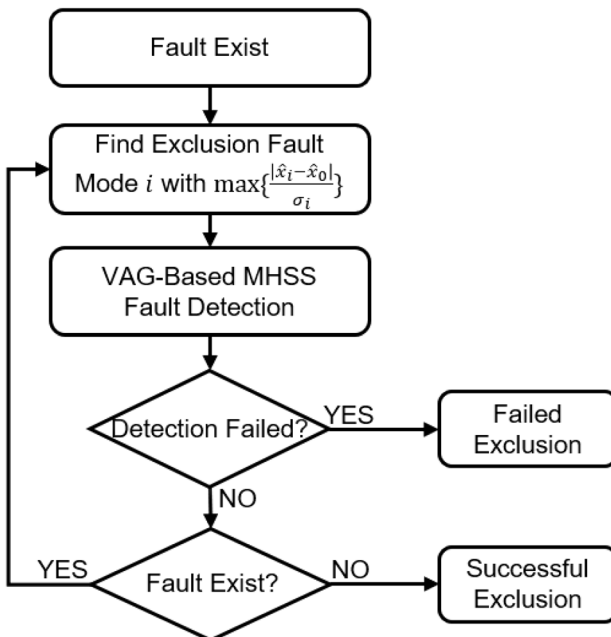


Fig. 5 Flowchart of VAG-Based MHSS fault exclusion. Once the fault is detected, MHSS fault exclusion can find the faulty measurements and obtain the fault-free positioning results

through flight testing. ARAIM mainly deals with satellite and constellation faults in the space segment. The fault-free error model in ARAIM is used to conservatively estimate the propagation error of GNSS signals (including multipath error, receiver error, etc.) (Wang et al. 2020). However, MHSS in urban areas mainly deals with multipath and NLOS faults. Since Real-Time Differential (RTD) positioning is utilized in the experimental section, the fault-free error model of MHSS in urban environment reflects the magnitude of random noise from GNSS receiver.

Since C/N_0 value determines how well the receiver tracking loops can track the signals and how precisely the receiver obtains pseudorange and carrier phase measurements (Won and Pany 2017; Issa et al. 2021), the fault-free error model for MHSS in urban environment is given by:

$$\sigma_{s,MP} = \sqrt{c_0 \times 10^{-\frac{(C/N_0)_s}{10}}} \quad (17)$$

where $c_0 = 1.1 \times 10^4 m^2 s^{-1}$ (Adjrad and Groves 2017). $\left(\frac{C}{N_0}\right)_s$ represents C/N_0 of satellite s in dB-Hz. Therefore, weight matrix \mathbf{W} in (2) is given by:

$$\mathbf{W} = \begin{bmatrix} \sigma_{1,MP}^{-2} & \dots & 0 & \dots & 0 \\ \vdots & \ddots & \vdots & \ddots & \vdots \\ 0 & \dots & \sigma_{s,MP}^{-2} & \dots & 0 \\ \vdots & \vdots & \vdots & \ddots & \vdots \\ 0 & \dots & 0 & \dots & \sigma_{N,MP}^{-2} \end{bmatrix} \quad (18)$$

Estimate $\hat{\mathbf{x}}_0$ can be obtained with (17) and (18).

VAG-based MHSS FDE with the enhancement of doppler test

Even if VAG is introduced to determine the fault mode in MHSS, fault detection process is still unable to monitor all possible fault modes in complex urban environments. In addition, VAG-Based MHSS fault exclusion always chooses the subset with the largest normalized test statistic as the exclusion option. However, for multiple-satellite faults, the optimal exclusion option may not have the largest normalized test statistic (Cassel 2017) leading to miss detection and wrong exclusion event. Since miss detection and wrong exclusion event result in large positioning deviation between the current epoch and previous epoch, the Doppler test is utilized to monitor the large deviation and help VAG-Based MHSS FDE find the optimal exclusion option.

Doppler shift measurement

Doppler shift is the frequency shift of electromagnetic signals caused by relative motion of GNSS user and satellite (He 2015).

With Doppler shift measurements output from GNSS receiver, velocity estimation accuracy can reach several centimeters per second (Wang and Xu 2011). Under fault-free condition, Doppler shift measurement $D_{s,t}$ at epoch t is given by:

$$D_{s,t} = \frac{1}{\lambda_f} \left[\mathbf{I}_{s,t} (\mathbf{v}_{s,t} - \mathbf{v}_{r,t}) + \dot{T}_{r,t}^s - \dot{I}_{r,t}^s + \epsilon_r^s \right] + \frac{c}{\lambda_f} (d_{r,t} - d_{s,t}) \quad (19)$$

where λ_f is the wavelength of GNSS signal. c is the speed of light. $d_{r,t}$ and $d_{s,t}$ are receiver clock drift and satellite clock drift, respectively. $\mathbf{v}_{s,t}$ and $\mathbf{v}_{r,t}$ are the 3×1 vectors representing the velocity of satellite s and receiver r at epoch t . $\mathbf{I}_{s,t}$ is the 1×3 unit line-of-sight vectors between GNSS satellite and receiver. ϵ_r^s is the un-modeled error rate, which can be considered as white Gaussian noise (WGN). $\dot{T}_{r,t}^s$ and $\dot{I}_{r,t}^s$ are tropospheric and ionospheric delay rate, respectively, which is ignored in a short time (Tu et al. 2018). Moreover, satellite clock drift is ignored in a short period of time due to its high stability (Hesselbarth and Wanninger 2008). Therefore, (19) can be rewritten as:

$$D_{s,t} = \frac{1}{\lambda_f} [\mathbf{I}_{s,t} (\mathbf{v}_{s,t} - \mathbf{v}_{r,t}) + \epsilon_r^s] + \frac{c}{\lambda_f} d_{r,t} \quad (20)$$

(20) is the simplified form of (19), which is used to calculate the Doppler residual in the next section.

Doppler test description

The Doppler test is introduced to measure the consistency of positioning results. The test statistic of the Doppler test at epoch t is calculated by the Doppler residual, which is given by:

$$res(t) = \lambda_f D_{s,t} - \hat{\mathbf{I}}_{s,t} (\hat{\mathbf{v}}_{s,t} - \hat{\mathbf{v}}_{r,t}) - c\tilde{d}_{r,t-1} \quad (21)$$

where $\hat{\mathbf{v}}_{s,t}$ and $\hat{\mathbf{v}}_{r,t}$ are the velocity estimation of satellite s and GNSS receiver. $\tilde{d}_{r,t-1}$ is the receiver clock drift estimated by Doppler shift measurements at epoch $t-1$, which is used to represent $d_{r,t}$. $\hat{\mathbf{I}}_{s,t}$ is the 1×3 unit line-of-sight vectors between GNSS satellite and the estimated location of receiver. Since the receiver clock drift is usually modeled as random walk (Angrisano 2010), $cd_{r,t}$ is given by:

$$cd_{r,t} = \eta_{drift} \quad (22)$$

where η_{drift} is the clock drift driving noise, which can be regarded as WGN. The discretization of (22) is represented by:

$$cd_{r,t} \approx cd_{r,t} - cd_{r,t-1} = \tilde{\eta}_{drift} \quad (23)$$

where $\tilde{\eta}_{drift}$ is the discretization noise. Assuming the difference between $\hat{\mathbf{I}}_{s,t}$ and $\mathbf{I}_{s,t}$ is small, by using (20) and (23), equation (21) is rewritten as:

$$res(t) = \mathbf{I}_{s,t} (\mathbf{v}_{s,t} - \hat{\mathbf{v}}_{s,t} - \mathbf{v}_{r,t} + \hat{\mathbf{v}}_{r,t}) + \epsilon_r^s + cd_{r,t-1} + \tilde{\eta}_{drift} - c\tilde{d}_{r,t-1} \quad (24)$$

where $\hat{\mathbf{v}}_{s,t}$ is calculated by broadcast ephemeris, and its bias and accuracy can reach the level of mm/s level (Remondi 2004). Since $\tilde{d}_{r,t-1}$ can represent the $d_{r,t-1}$, according to (23), (24) is rewritten as:

$$res(t) = \mathbf{I}_{s,t} (\mathbf{v}_{s,t} - \hat{\mathbf{v}}_{s,t} - \mathbf{v}_{r,t} + \hat{\mathbf{v}}_{r,t}) + \epsilon_r^s + \tilde{\eta}_{drift} \quad (25)$$

The test statistic of the Doppler test can be obtained by (25).

If GNSS measurements are fault free, we assume the measurement noise obeys WGN with a mean of zero. Since WLS is an unbiased estimation, the mean of $res(t)$ is zero. Assuming that the un-modeled error is small and the receiver clock is stable, ϵ_r^s and $\tilde{\eta}_{drift}$ can be ignored compared with the measurement noise. Therefore, the variance of $res(t)$ mainly depends on $\mathbf{v}_{r,t} - \hat{\mathbf{v}}_{r,t}$ term, which is given by:

$$D(res(t)) = E(\mathbf{I}_{s,t} \cdot \hat{\mathbf{v}}_{r,t}) \cdot (\mathbf{I}_{s,t} \cdot \hat{\mathbf{v}}_{r,t})^T = E(\mathbf{I}_{s,t} \hat{\mathbf{v}}_{r,t} \hat{\mathbf{v}}_{r,t}^T \mathbf{I}_{s,t}^T) \quad (26)$$

where $\hat{\mathbf{v}}_{r,t}$ can be represented by the position estimation of two adjacent epochs, which is given by:

$$\hat{\mathbf{v}}_{r,t} = \frac{1}{\Delta T} (\hat{\mathbf{x}}_t - \hat{\mathbf{x}}_{t-1}) \quad (27)$$

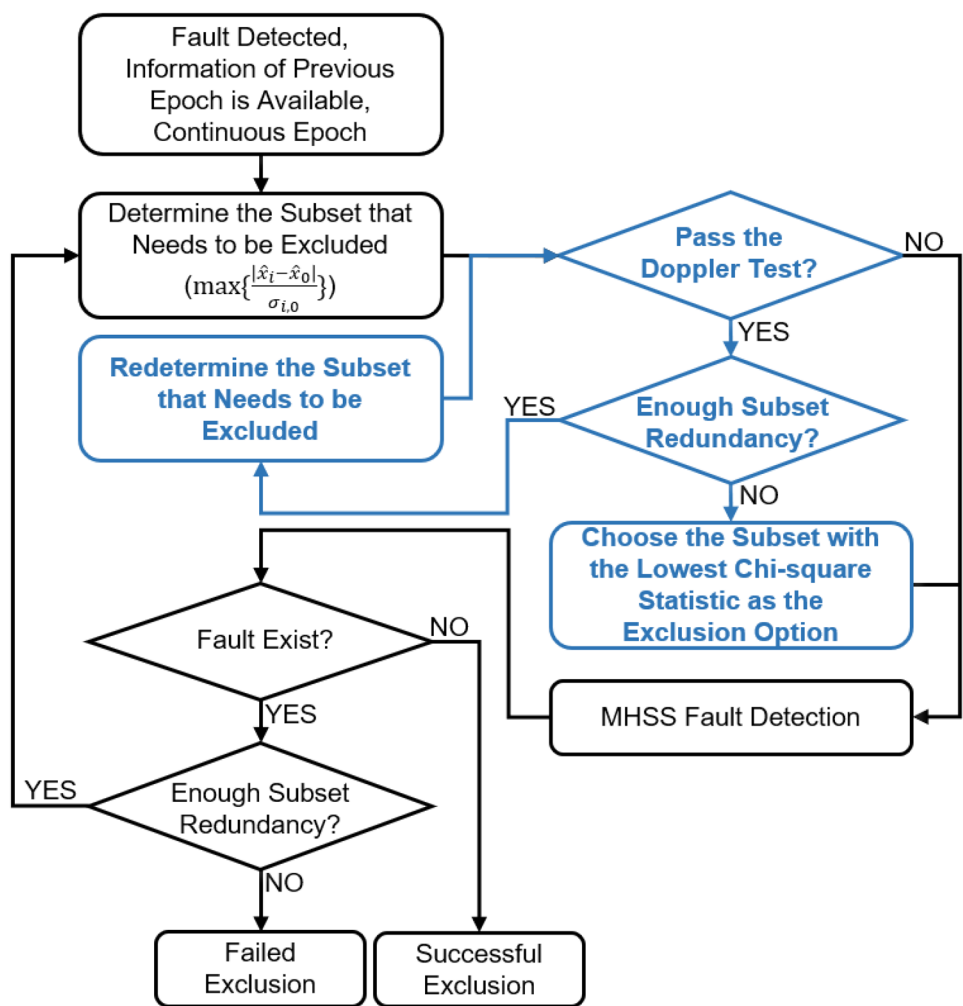
where ΔT is the time between epoch t and $t-1$. Based on (27) and (2), (26) is rewritten as:

$$\begin{aligned} D(res(t)) &= \mathbf{I}_{s,t} E \left(\frac{1}{\Delta T} (\hat{\mathbf{x}}_t - \hat{\mathbf{x}}_{t-1}) \frac{1}{\Delta T} (\hat{\mathbf{x}}_t - \hat{\mathbf{x}}_{t-1})^T \right) \mathbf{I}_{s,t}^T \\ &= \frac{1}{\Delta T^2} \mathbf{I}_{s,t} \mathbf{S}_t \mathbf{W}_t \mathbf{S}_t^T \mathbf{I}_{s,t}^T + \frac{1}{\Delta T^2} \mathbf{I}_{s,t} \mathbf{S}_{t-1} \mathbf{W}_{t-1} \mathbf{S}_{t-1}^T \mathbf{I}_{s,t}^T \\ &= \frac{1}{\Delta T^2} \mathbf{I}_{s,t} (\mathbf{cov}_t + \mathbf{cov}_{t-1}) \mathbf{I}_{s,t}^T \end{aligned} \quad (28)$$

where subscript t represents epoch t . In (28), the definition of \mathbf{S}_t is the same as \mathbf{S}_0 in (2). The definition of \mathbf{W}_t is the same as weight matrix \mathbf{W} in (2). \mathbf{cov}_t represents the covariance matrix of position estimation. Then Doppler test is introduced based on Chi-square test statistic χ_{res}^2 , which is given by:

$$\chi_{res}^2(n-4) = \sum_{i=1}^{i=n} \frac{res(t)_i^2}{D(res(t)_i)^2} \quad (29)$$

Fig. 6 Flowchart of D-FE. The blue part of this flowchart represents the process of redetermining the exclusion option based on the Doppler test



where $n - 4$ are the degrees of freedom of Chi-square distribution.

FDE with the enhancement of doppler test

In urban areas, multiple measurement faults may exist in the observable, causing the VAG-Based MHSS FDE to fail. For VAG-Based MHSS fault detection, it requires enough fault-free satellites to detect the measurement fault. However, when multiple measurement faults occur, this requirement cannot be satisfied, which leads to a miss detection event. For VAG-Based MHSS fault exclusion, when multipath/NLOS errors contaminate most of the GNSS measurements, the test statistic after excluding fault-free subset can still pass the VAG-Based MHSS fault detection, which leads to a wrong exclusion event.

The miss detection and wrong exclusion event can lead to large positioning error. Since the user motion is continues, and if the positioning error of the previous epoch is small, the user location at the current epoch cannot deviate far from

that of the previous epoch. Test statistics of the Doppler test calculated by Doppler shift measurements are used to monitor the large deviation of the user position.

We first introduce Doppler test-enhanced fault exclusion to improve the effectiveness of VAG-Based MHSS fault exclusion (D-FE). The flowchart of D-FE is shown in Fig. 6. In Fig. 6, D-FE utilizes Doppler test to determine the exclusion option. Compared with VAG-Based MHSS fault exclusion, the exclusion option determined by D-FE considers the continuity of the user motion. When all the Chi-square test statistics cannot pass the Doppler test, D-FE chooses the fault mode with the lowest Chi-square statistic as the exclusion option. This means the selection of the exclusion option is based on the principle that the positioning result of D-FE cannot deviate far from previous results. As to the satellite redundancy, D-FE needs at least eight satellites to operate for three-constellation positioning. In Fig. 6, under the premise that measurement fault is detected, D-FE is carried out with the previous information. The previous information refers to \hat{x}_{t-1} , cov_{t-1} in (28) and receiver clock drift estimation of the previous epoch.

Before introducing the Doppler test-enhanced FDE scheme, we first introduce velocity integral. The purpose of the velocity integral is to provide positioning results when satellite redundancy is insufficient or the fault exclusion process fails to exclude the measurement fault. The positioning result $\hat{x}_{VI,t}$ and its covariance matrix $\text{cov}_{VI,t}$ are the results of velocity integral, which can be expressed as (Li et al. 2018):

$$\begin{cases} \hat{x}_{VI,t} = \hat{x}_{t-1} + \hat{v}_{e,t-1} \cdot \Delta T \\ \text{cov}_{VI,t} = \text{cov}_{t-1} + \text{cov}_{\hat{v}_{e,t-1}} \cdot \Delta T^2 \end{cases} \quad (30)$$

where $\hat{v}_{e,t-1}$ is the velocity estimation at epoch $t - 1$. $\text{cov}_{\hat{v}_{e,t-1}}$ is the covariance matrix of $\hat{v}_{e,t-1}$.

Doppler test-enhanced FDE scheme is shown in Fig. 7. Doppler test-enhanced fault detection (D-FD) is also introduced in Fig. 7. D-FD is used to detect measurement fault

when VAG-Based MHSS fault detection fails to detect the faulty measurements. Moreover, the Update function in Fig. 7 is to calculate the \hat{x}_t , $d_{r,t}$, cov_t , $\hat{v}_{e,t}$ and $\text{cov}_{\hat{v}_{e,t}}$ at epoch t for Doppler test or velocity integral in the next epoch. $\hat{v}_{e,t}$, $\text{cov}_{\hat{v}_{e,t}}$ and $d_{r,t}$ can be estimated by WLS with Doppler measurements.

Moreover, when velocity integral is used, it means the faulty measurements cannot be excluded by D-FE and the estimation results of \hat{x}_t , $d_{r,t}$, cov_t , $\hat{v}_{e,t}$ and $\text{cov}_{\hat{v}_{e,t}}$ are incorrect. In this case, for the Update function, \hat{x}_t and cov_t are equal to $\hat{x}_{VI,t}$ and $\text{cov}_{VI,t}$, respectively. As to $d_{r,t}$, $\hat{v}_{e,t}$ and $\text{cov}_{\hat{v}_{e,t}}$, their values are the same as the corresponding values from the previous Update function. For velocity integral, the positioning accuracy decreases significantly when the integration time is too long. Therefore, proposed

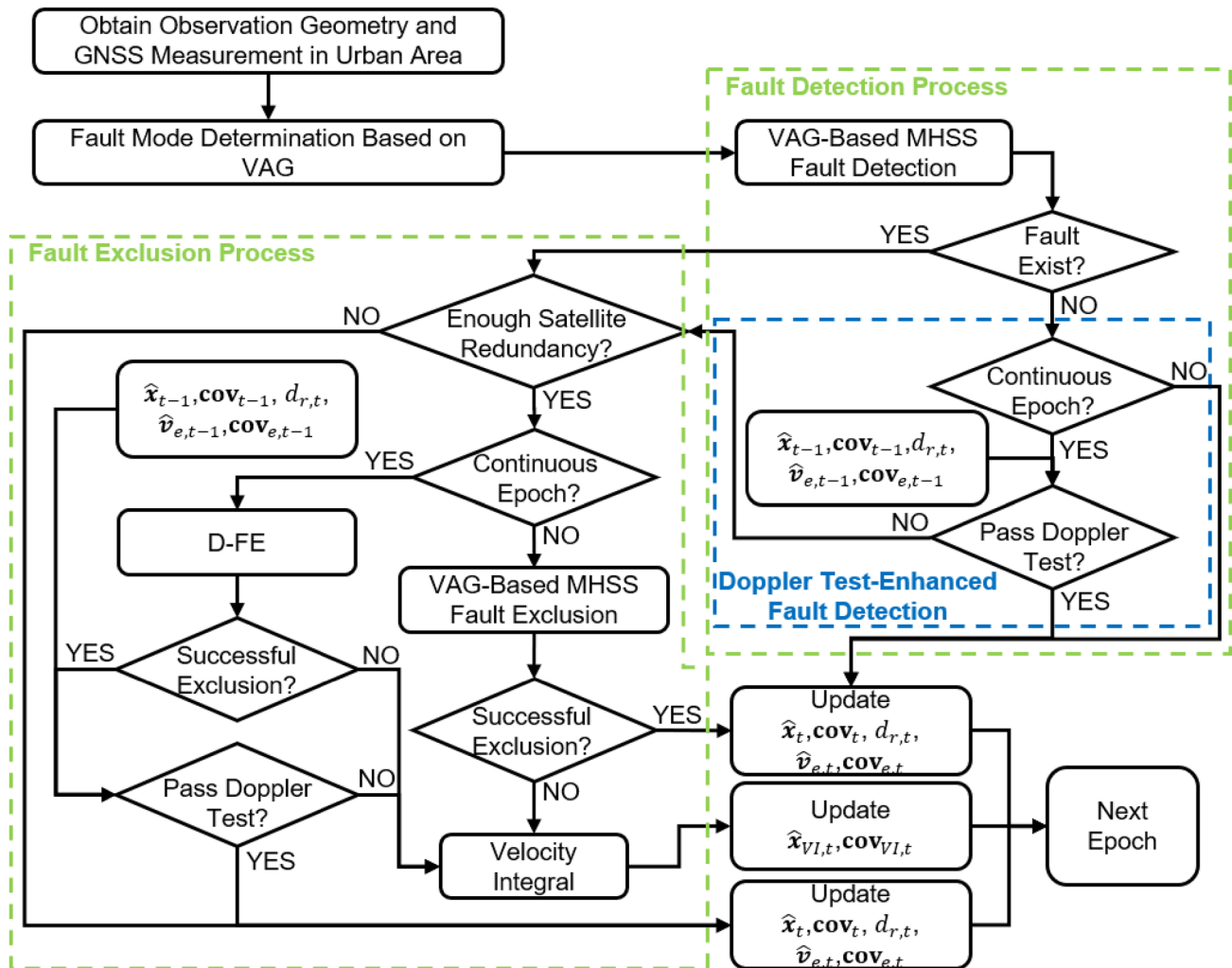


Fig. 7 Flowchart of Doppler test-enhanced FDE scheme. The blue dotted box is the D-FD. The green dotted boxes represent the process of faulty GNSS measurement detection and exclusion process. Dop-

pler test-enhanced FDE scheme combines Doppler test and VAG-Based MHSS FDE

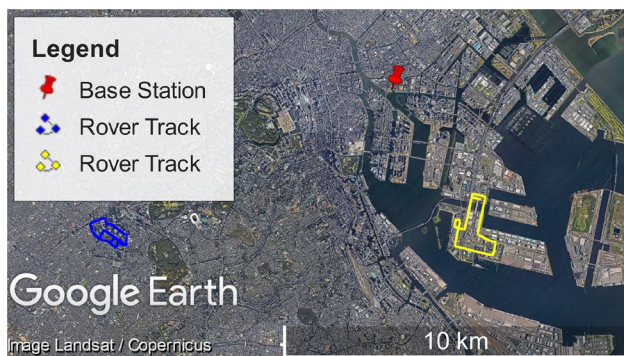


Fig. 8 Base station and rover track in Odaiba and Shinjuku

velocity integral function is suitable for case of short integration time.

Experiments and results

The experiments are carried out based on the open-source dataset, UrbanNav, which is from Intelligent Positioning and Navigation Laboratory of Hong Kong Polytechnic University. The dataset contains RINEX files of rover and base station with a sampling interval of 0.1 s and ground truth files collected from Odaiba and Shinjuku in Tokyo on December 19, 2018. The rover track and the location of base station are shown in Fig. 8. In our experiments, three-constellation (GPS, BDS and GLONASS) Real-Time Differential (RTD) positioning is used to validate the effectiveness of proposed Doppler test-enhanced FDE scheme.

Parameter settings

Doppler test-enhanced FDE scheme needs to determine three parameters in advance: CCV, false alert probability for VAG-Based MHSS fault detection and Doppler test. CCV is crucial for VAG. Different CCVs correspond to different fault modes used in Doppler test-enhanced FDE. Setting CCV ensures that the multipath/NLOS difference of satellites satisfying the predefined CCV remains a small value. Figure 2 shows that the multipath/NLOS difference reaches the minimum when CCV equals 0.95. Sensitivity analysis is then applied to determine the appropriate value of CCV. For the false alert probability in VAG-Based MHSS fault detection, Doppler test and Consistency Check, it equals 1×10^{-6} . In addition, since RTD is utilized, the value of b_{norm} can be significantly decreased, which is predefined as 0 in the following experiment.

Evaluation in Odaiba

Figure 9 shows satellite visibility in Odaiba, which indicates that 91% of the data satisfies the VAG-Based MHSS fault detection requirement. Moreover, when CCV is set to different values (0.95, 0.97, 0.99), the maximum integration time is analyzed, which is 7 s in Odaiba.

The results of sensitivity analysis are shown in Table 1. Table 1 evaluates the 3D mean value, 3D STD, 3D maximum undetected error and execution time. Table 1 indicates that whether CCV is set to 0.95, 0.97 or 0.99, the Doppler test-enhanced FDE results do not change significantly.

According to sensitivity analysis, CCV is set to 0.95. We then compare Doppler test-enhanced FDE with Consistency Check. The results of the Doppler test-enhanced FDE and Consistency Check are shown in Table 2. Table 2 indicates that Doppler test-enhanced FDE not only has the smaller undetected error than Consistency Check but also significantly reduces the positioning error caused by multipath/NLOS effects. Table 2 demonstrates that Doppler test-enhanced FDE can reduce the mean positioning error by 24% and improve the positioning accuracy by 59%.

Figure 10 depicts the detection results of Doppler test-enhanced FDE and Consistency Check. In Fig. 10, the blue line is the positioning error of RTD. As illustrated in Fig. 10

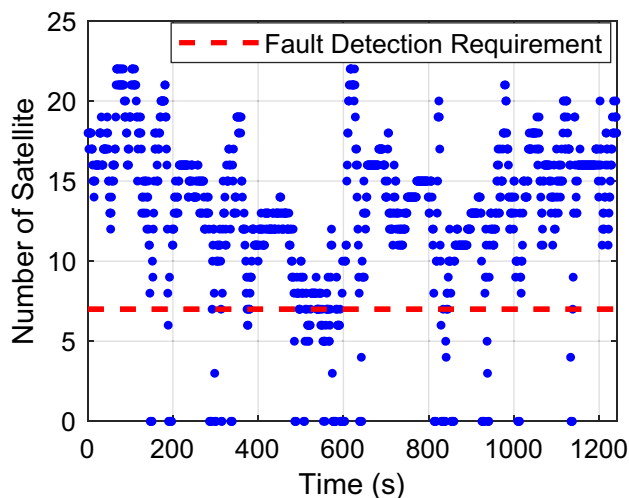


Fig. 9 Satellite visibility in Odaiba

Table 1 Sensitivity analysis of different CCV in Odaiba

| CCV | Mean value (m) | STD (m) | Maximum undetected error (m) | Time (s) |
|------|----------------|---------|------------------------------|----------|
| 0.95 | 5.27 | 6.28 | 41.92 | 399 |
| 0.97 | 5.32 | 6.50 | 41.92 | 403 |
| 0.99 | 5.29 | 6.47 | 41.92 | 402 |

Table 2 Positioning results of doppler test-enhanced FDE and consistency check in Odaiba

| Mode | Mean value (m) | STD (m) | Maximum undetected error (m) | Time (s) |
|---------------------------|----------------|---------|------------------------------|----------|
| WLS | 14.56 | 37.86 | — | — |
| Consistency Check | 7.31 | 16.53 | 118.57 | 358 |
| Doppler test-enhanced FDE | 5.27 | 6.28 | 41.92 | 399 |

top plane, red and green dots denote the faulty epochs detected by VAG-Based MHSS fault detection and D-FD, respectively. As shown in Fig. 10 bottom plane, red dots denote the faulty epochs detected by Consistency Check. The results show that Doppler test-enhanced FDE is able to detect more GNSS faults than Consistency Check.

Exclusion results of the Doppler test-enhanced FDE and Consistency Check are given in Fig. 11. As shown in Fig. 11 (top), the blue line is the positioning error of Doppler test-enhanced FDE. Red, green and navy-blue dots are exclusion results computed by D-FE, VAG-Based MHSS fault exclusion and velocity integral. As illustrated

in the bottom plane, the blue line is the positioning error of Consistency Check exclusion. Red dots are exclusion results computed by Consistency Check exclusion. Compared with RTD results in Fig. 10, Fig. 11 shows that the positioning error can be significantly decreased by using Doppler test-enhanced FDE.

Figure 12 depicts the bird view of positioning results in Odaiba. In Fig. 12, the yellow line is the ground truth of the rover track. The red line is the original positioning result of RTD. The green dotted line and blue dotted lines are the exclusion results of Doppler test-enhanced FDE and Consistency Check, respectively.

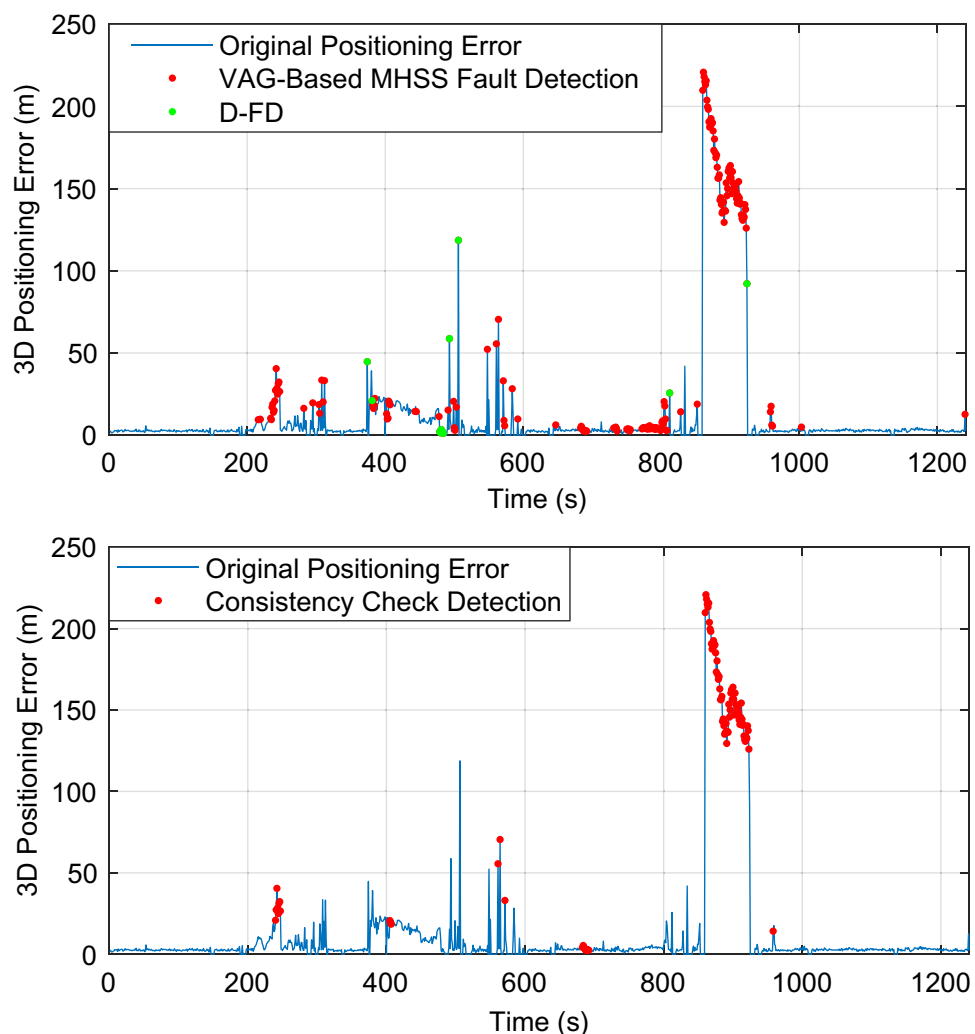
Fig. 10 Detection results of Doppler test-enhanced FDE in Odaiba (top panel), and Consistency Check detection result in Odaiba (bottom panel)

Fig. 11 Exclusion results of Doppler test-enhanced FDE in Odaiba (top), and Consistency Check exclusion result in Odaiba (bottom)

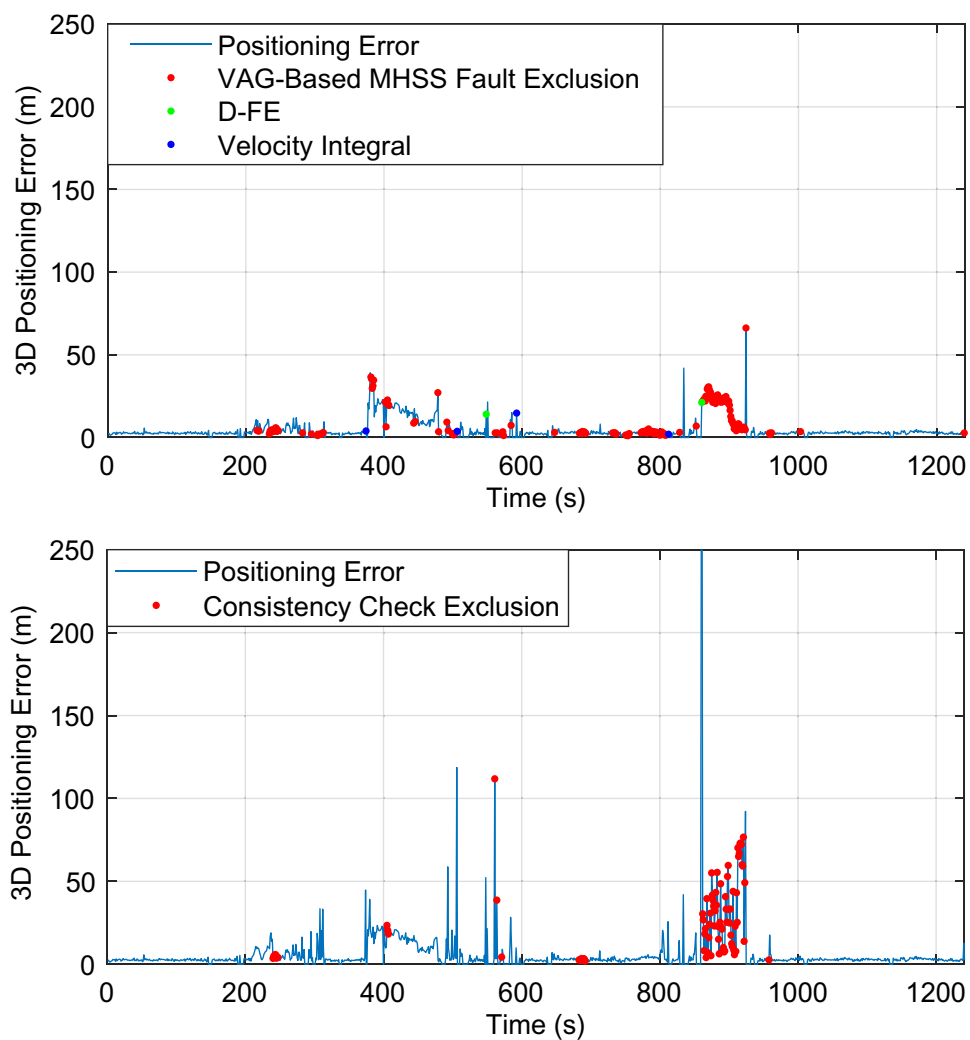


Fig. 12 Bird view of positioning results in Odaiba

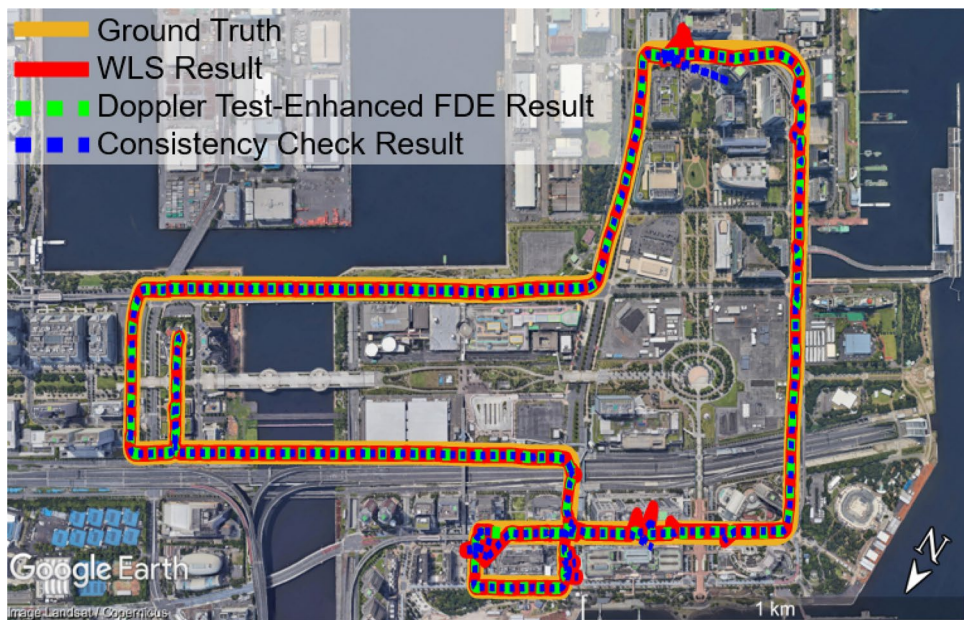


Fig. 13 A comprehensive performance comparison among two methods in Odaiba

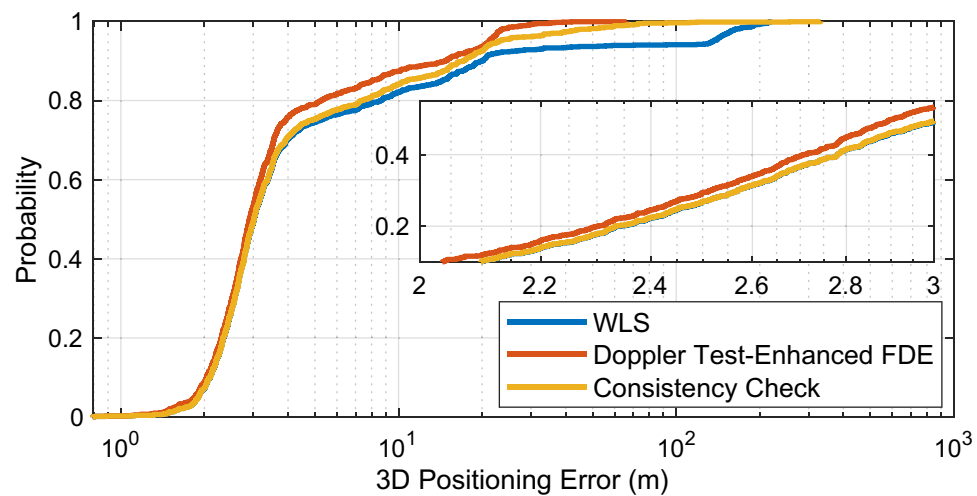


Table 3 Sensitivity analysis of different CCV in Shinjuku

| CCV | Mean value (m) | STD (m) | Maximum undetected error (m) | Time (s) |
|------|----------------|---------|------------------------------|----------|
| 0.95 | 6.15 | 8.70 | 34.75 | 402 |
| 0.97 | 5.89 | 8.11 | 34.75 | 410 |
| 0.99 | 5.96 | 8.11 | 34.75 | 406 |

In addition, Fig. 13 provides the view of performance comparison among Doppler test-enhanced FDE and Consistency Check in Odaiba. Positioning error is presented in the form of Cumulative Distribution Function (CDF). It shows that employing Doppler test-enhanced FDE can improve the 3D positioning accuracy of RTD.

Evaluation in Shinjuku

Figure 14 shows satellite visibility in Shinjuku, indicating that 84% of the data in Shinjuku satisfies the VAG-Based MHSS fault detection requirement. Moreover, when CCV is set to different values (0.95, 0.97, 0.99), the maximum integration time is analyzed, which is 125 s in Shinjuku (between 1500 and 1700 s). Since proposed Doppler test-enhanced FDE is suitable for situations with short integration time, the following analysis only considers data within 1500 s.

Table 4 Positioning results of Doppler test-enhanced FDE and consistency check in Shinjuku

| Mode | Mean value (m) | STD (m) | Maximum undetected error (m) | Time (s) |
|---------------------------|----------------|---------|------------------------------|----------|
| WLS | 15.59 | 30.10 | – | – |
| Consistency Check | 11.16 | 24.94 | 186.84 | 368 |
| Doppler test-enhanced FDE | 6.15 | 8.70 | 34.75 | 402 |

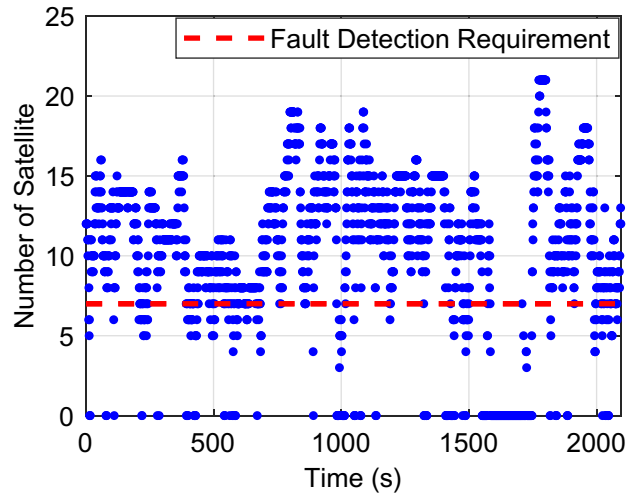
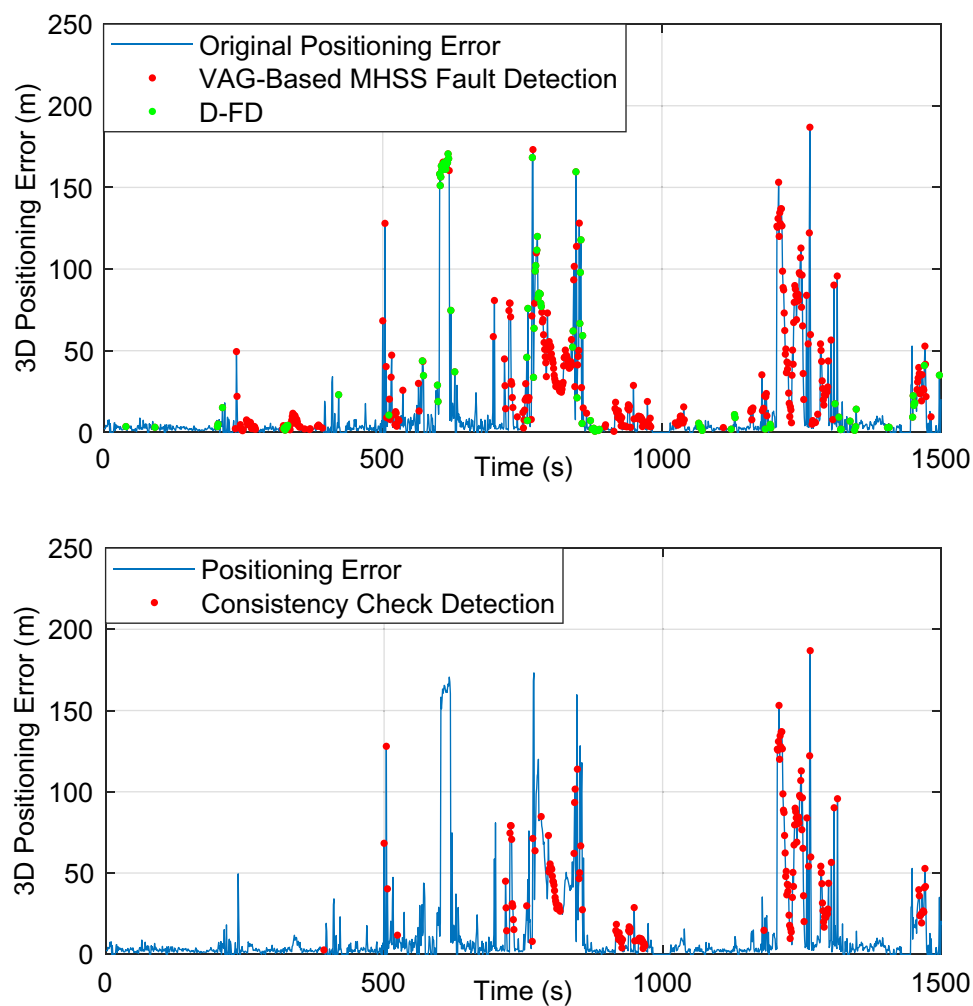


Fig. 14 Satellite visibility in Shinjuku

The results of sensitivity analysis are shown in Table 3. Table 3 evaluates the 3D mean value, 3D STD, 3D maximum undetected error and execution time. Table 3 indicates that whether CCV is set to 0.95, 0.97 or 0.99, the Doppler test enhanced FDE results do not change significantly.

Based on sensitivity analysis, CCV is set to 0.95. We then compare Doppler test-enhanced FDE with Consistency Check method. The results of the Doppler test-enhanced

Fig. 15 Detection results of Doppler test-enhanced FDE in Odaiba (top panel), and Consistency Check detection result in Odaiba (bottom panel)



FDE and Consistency Check are shown in Table 4. Table 4 indicates that Doppler test-enhanced FDE is not only has the smaller undetected error than Consistency Check but also significantly improves the position accuracy. Table 4 demonstrates that Doppler test-enhanced FDE can reduce the mean positioning error by 44% and improve the positioning accuracy by 53%.

Figure 15 depicts the detection results of the Doppler test-enhanced FDE and Consistency Check. The blue line is the positioning error of RTD. In the top plane, the red and green dots denote the faulty epochs detected by VAG-Based MHSS fault detection and D-FD, respectively. In the bottom plane, the red dots denote the faulty epochs detected by Consistency Check. The results show that Doppler test-enhanced FDE is able to detect more GNSS faults than Consistency Check.

Exclusion results of Doppler test-enhanced FDE and Consistency Check are given in Fig. 16. As shown in Fig. 16 top plane, the blue line is positioning error of Doppler test-enhanced FDE. Red, green and navy-blue dots are exclusion results computed by D-FE, VAG-Based MHSS fault exclusion and velocity integral. As illustrated in Fig. 16 bottom

plane, the blue line is the positioning error of Consistency Check exclusion. Red dots are exclusion results computed by Consistency Check exclusion. Compared with RTD results in Fig. 15, Fig. 16 shows that the positioning error can be significantly decreased by using Doppler test-enhanced FDE.

Figure 17 depicts the bird view of positioning results in Shinjuku. In Fig. 17, the yellow line is the ground truth of the rover track. The Red line is the original positioning result of RTD. The green dotted line and blue dotted line are the exclusion results of the Doppler test-enhanced FDE and Consistency Check.

In addition, Fig. 18 provides the view of performance comparison among Doppler test-enhanced FDE and Consistency Check in Shinjuku. Positioning error is presented in the form of cumulative distribution function (CDF). It shows that employing Doppler test-enhanced FDE can improve the 3D positioning accuracy of RTD.

Fig. 16 Exclusion results of Doppler test-enhanced FDE in Shinjuku (top panel), and Consistency Check exclusion result in Shinjuku (bottom panel)

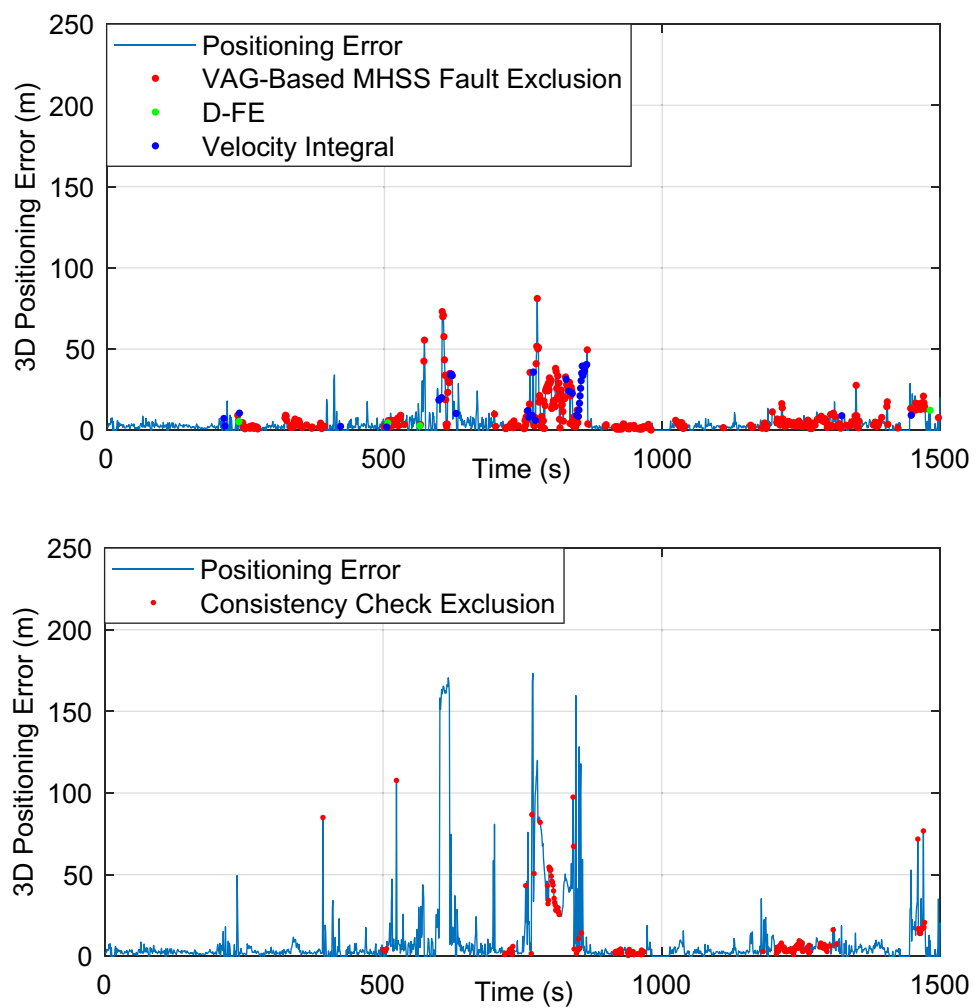


Fig. 17 Bird view of positioning results in Shinjuku

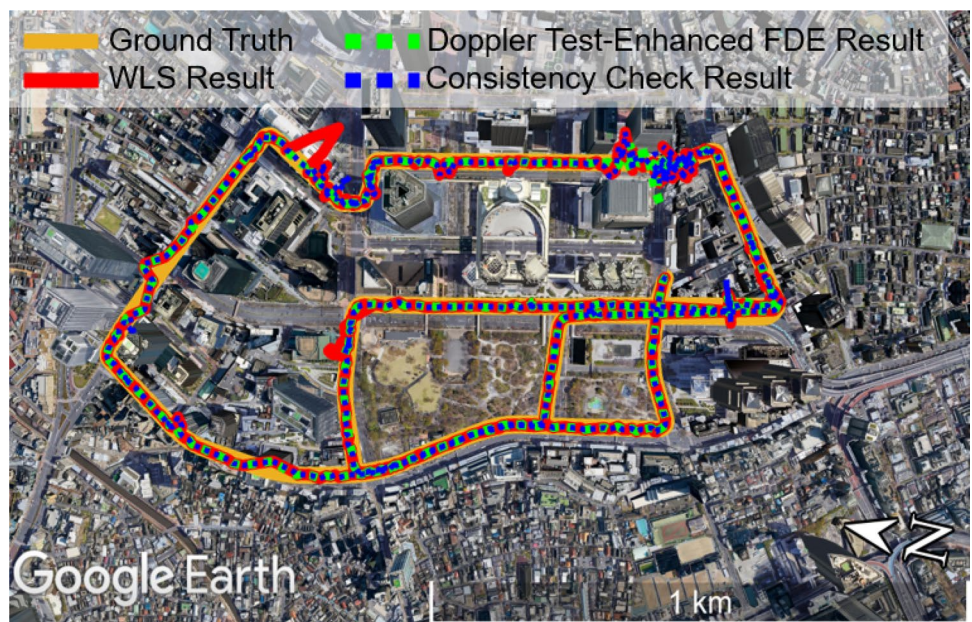
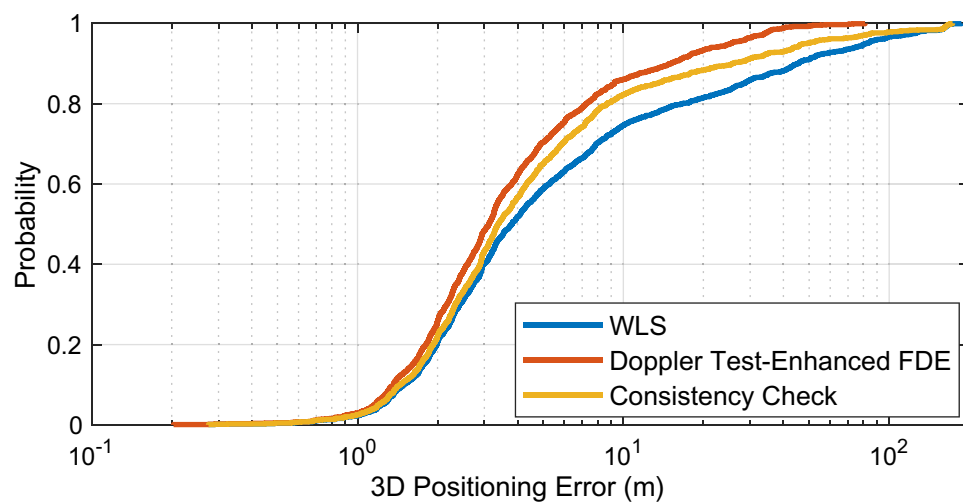


Fig. 18 Comprehensive performance comparison among two methods in Shinjuku



Conclusion

To improve GNSS performance in urban areas, we propose the Doppler test-enhanced fault detection and exclusion (FDE) to detect and exclude faulty GNSS measurements interfered by multipath/NLOS effects. Doppler test-enhanced FDE mainly contains vector angle grouping-based (VAG-based) multiple hypothesis solution separation (MHSS) FDE and the Doppler test. In Doppler test-enhanced FDE, VAG-based MHSS FDE is able to monitor the multiple GNSS measurement fault in urban areas, and the Doppler test is designed to avoid the miss detection and wrong exclusion event of Doppler test-enhanced FDE. With Doppler test-enhanced FDE, GNSS performance can be greatly improved.

According to real-time dataset analysis in Odaiba and Shinjuku, compared with Consistency Check, the introduction of Doppler test-enhanced FDE not only diminishes the undetected error but also significantly improves the positioning accuracy and precision. In Odaiba and Shinjuku, when Doppler test-enhanced FDE is introduced, the mean positioning error is reduced by 24% and 44%, respectively. The positioning accuracy is increased by 44% and 53%, respectively.

Although the undetected error of Doppler test-enhanced FDE is smaller than Consistency Check, some epochs with small positioning error are still marked as faulty epoch. This is because the fault-free error model is too conservative. Since the correctness of Solution Separation detection is related to fault-free error models in urban areas, the more accurate error model for Doppler test-enhanced FDE will be determined in future work.

Acknowledgements This research was jointly supported by the National Natural Science Foundation of China (Nos. 62173227,

62103274, 62003211) and the Shanghai Pujiang Program (No. 20PJ1409100).

Data availability The data sets used in this study are from <https://github.com/IPNL-POLYU/UrbanNavDataset>.

References

- Adjrad M, Groves PD (2017) Enhancing least squares GNSS positioning with 3D mapping without accurate prior knowledge. *Navigation* 64(1):75–91
- Angrisano A (2010) GNSS/INS integration methods. Doctoral dissertation, The University of Calgary Schulich School of Engineering
- Blanch J, Walter T, Enge P, Lee Y, Spletter A (2012) Advanced RAIM user algorithm description: integrity support message processing, fault detection, exclusion, and protection level calculation. Proc. ION GNSS 2012, Institute of Navigation, Nashville, Tennessee, USA, September 17–21: 2828–2849
- Borre K (2007) A software-defined GPS and Galileo receiver: a single-frequency approach. Springer, Berlin
- Cassel R (2017) Real-Time ARAIM Using GPS, GLONASS, and GALILEO. Ph.D. thesis, http://www.navlab.iit.edu/uploads/5/9/7/3/59735535/thesis_final.pdf.
- Dierendonck AV, Fenton P, Ford T (1992) Theory and performance of narrow correlator spacing in a GPS receiver. *Navigation* 39(3):265–283
- Grewal MS, Weill LR, Andrews AP (2007) Global positioning systems, inertial navigation, and integration. Wiley, New York
- Hesselbarth A, Wanninger L (2008) Short-term stability of GNSS satellite clocks and its effects on precise point positioning. Proc. ION GNSS 2008, Institute of Navigation, Savannah, GA, USA, September 16–19: 1855–1863
- He K (2015) GNSS kinematic position and velocity determination for airborne gravimetry. Doctoral dissertation, Deutsches GeoForschungsZentrum GFZ Potsdam.
- Hofmann-Wellenhof B, Lichtenegger H, Wasle E (2007) GNSS—global navigation satellite systems: GPS, GLONASS, Galileo, and more. Springer, Berlin
- Hsu LT (2018) Analysis and modeling GPS NLOS effect in highly urbanized area. *GPS Solutions* 22(7):1–12

- Hsu LT, Tokura H, Kubo N, Gu Y, Kamijo S (2017) Multiple faulty GNSS measurement exclusion based on Consistency Check in urban canyons. *IEEE Sens J* 17(6):1909–1917
- Issa H, Stienne G, Reboul S, Semmling M, Raad M, Faour G, Wickert J (2021) A probabilistic model for on-line estimation of the GNSS carrier-to-noise ratio. *Signal Process* 184(4):107992
- Joerger M, Chan FC, Pervan B (2014) Solution separation versus residual-based RAIM. *Navigation* 61(4):273–291
- Karaim M, Elsheikh M, Noureldin A (2018) GNSS error sources. In: Rustamov RB, Hashimov AM (eds) *Multifunctional operation and application of GPS*. IntechOpen, London, pp 69–85
- Li X, Guo JM, Zhang D, Yang F (2018) An algorithm of GPS single-epoch kinematic positioning based on doppler velocimetry. *Geomatics Inf Sci Wuhan Univ* 43(007):1036–1041
- Marais J, Berbineau M, Heddebaud M (2005) Land mobile GNSS availability and multipath evaluation tool. *IEEE Trans Veh Technol* 54(5):1697–1704
- McGraw GA, Groves PD, Ashman BW (2019) Robust positioning in the presence of multipath and NLOS GNSS signals. Wiley, Hoboken
- McGraw GA, Groves PD, Ashman BW (2020) Robust positioning in the presence of multipath and NLOS GNSS signals. In: Morton J, Diggelen VF, Spilker J, Parkinson WB, Lo SM, Gao G (eds) *Position, navigation, and timing technologies in the 21st century: integrated satellite navigation, sensor systems, and civil applications*, vol 1. Wiley, Hoboken, pp 551–589
- Meguro J, Murata T, Takiguchi J, Amano Y, Hashizume T (2009) GPS multipath mitigation for urban area using omnidirectional infrared camera. *IEEE Trans Intell Transp Syst* 10(1):22–30
- Morales, L.G. (2011). Adaptive filtering applications. BoD-books on demand.
- Pan W, Zhan X, Zhang X (2019) Fault exclusion method for ARAIM based on tight GNSS/INS integration to achieve CAT-I approach. *IET Radar Sonar Navig* 13(11):1909–1917
- Pervan BS, Pullen SP, Christie JR (1998) Multiple hypothesis approach to satellite navigation integrity. *Navigation* 45(1):61–71
- Remondi BW (2004) Computing satellite velocity using the broadcast ephemeris. *GPS Solut* 8(3):181–183
- Strode PR, Groves PD (2016) GNSS multipath detection using three-frequency signal-to-noise measurements. *GPS Solut* 20(3):399–412
- Suzuki T (2019) Mobile robot localization with GNSS multipath detection using pseudorange residuals. *Adv Robot* 33(12):602–613
- Tu J, Zhan X, Zhang X, Zhang Z, Jing S (2018) Low-complexity GNSS anti-spoofing technique based on Doppler frequency difference monitoring. *IET Radar Sonar Navig* 12(9):1058–1065
- Walter T, Blanch J, Gunning K, Joerger M, Pervan B (2019) Determination of fault probabilities for ARAIM. *IEEE Trans Aerosp Electron Syst* 55(6):3505–3516
- Wang Q, Xu T (2011) Combining GPS carrier phase and Doppler observations for precise velocity determination. *Sci China Phys Astron* 54:1022–1028
- Wang S, Zhan X, Zhai Y, Liu B (2020) Fault detection and exclusion for tightly coupled GNSS/INS system considering fault in state prediction. *Sensors* 20(3):590
- Won J, Pany T (2017) Signal processing. In: Teunissen PJ, Montenbruck O (eds) *Springer handbook of global navigation satellite systems*. Springer, Cham
- Zhang G, Wen W, Hsu LT (2019a) Rectification of GNSS-based collaborative positioning using 3D building models in urban areas. *GPS Solut* 23(3):83
- Zhai Y, Joerger M, Pervan B (2018) Fault exclusion in multi-constellation global navigation satellite systems. *J Navig* 71(6):1281–1298
- Zhai Y, Patel J, Zhan X, Joerger M, Pervan B (2020) An advanced receiver autonomous integrity monitoring (ARAIM) ground

monitor design to estimate satellite orbits and clocks. *Navigation* 73(5):1087–1105

- Zhang Z, Li B, Yang G, Shen Y (2019b) Real-time carrier phase multipath detection based on dual-frequency C/N0 data. *GPS Solut* 23(1):7

Publisher's Note Springer Nature remains neutral with regard to jurisdictional claims in published maps and institutional affiliations.

Springer Nature or its licensor holds exclusive rights to this article under a publishing agreement with the author(s) or other rightsholder(s); author self-archiving of the accepted manuscript version of this article is solely governed by the terms of such publishing agreement and applicable law.



Jin Chang is currently a Master's student at the School of Aeronautics and Astronautics, Shanghai Jiao Tong University (SJTU). His research interests focus on multipath mitigation and GNSS integrity monitoring algorithms.



Xingqun Zhan received his Ph.D. from Harbin Institute of Technology (HIT), China, in 1999 and is currently a professor and the associate dean of the School of Aeronautics and Astronautics at Shanghai Jiao Tong University (SJTU). His research interests focus on navigation integrity, multi-sensor integration, and cooperative navigation.



Yawei Zhai obtained his Ph.D. in Mechanical and Aerospace Engineering from the Illinois Institute of Technology, USA, in 2018 and is currently a post-doctoral researcher at Shanghai Jiao Tong University (SJTU). His research focuses on Advanced Receiver Autonomous Integrity Monitoring (ARAIM) and multi-sensor integration.



Shizhuang Wang is currently a Ph.D. student at the School of Aeronautics and Astronautics, Shanghai Jiao Tong University (SJTU). His research interests focus on navigation integrity and multi-sensor integration.



Rong Yang is an assistant professor in the School of Aeronautics and Astronautics, Shanghai Jiao Tong University, China. She received her Ph.D. at Nanyang Technological University and was a Research Associate at the University of Colorado, Boulder. Her research focuses on GNSS signal processing for navigation in challenging environments.



Kui Lin received his Ph.D. from the School of Aeronautics and Astronautics at Shanghai Jiao Tong University (SJTU). His research interests focus on the interoperable GNSS Space Service Volume.